Lunar Navigation Performance using the Deep Space Network and Alternate Solutions to Support Precision Landing

Bradley C. Collicott* and David C. Woffinden†
NASA Johnson Space Center, Houston, TX, 77573

As human exploration once again targets the surface of the Moon, questions continue to emerge regarding the necessity of Earth-based tracking systems, such as the Deep Space Network, for spacecraft navigation in support of lunar descent and landing. This paper will derive an extensive Deep Space Network sensor model for use in linear covariance analysis and demonstrate the resulting trajectory dispersions and navigation performance in comparison with alternate solutions, such as terrain relative navigation. An in-depth trade study with considerations for various trajectory profiles, time allocated to ground tracking, number of active ground stations, and interaction with other sensors will be conducted to shed significant insight into sensor suite requirements to ensure safe and precise landing on the Moon.

I. Introduction

The use of radiometric tracking in spacecraft navigation has a rich history that antedates even the first human landing on the Moon, beginning with the establishment of the Deep Space Network (DSN) in 1958 to communicate with the Explorer 1 spacecraft [1]. As human presence in space expanded, so did the DSN; with locations in California, Madrid, and Austrailia, the network is capable of providing nearly unfettered coverage to spacecraft beyond low-Earth orbit (LEO). However, increased space mission volume has created concerns about future expectations of DSN usage for spacecraft navigation, including support for lunar landings [2]. As the DSN continues accepting new tracking responsibilities in addition to supporting legacy projects (some that are significantly out-living expectations), alternative solutions are being explored to ensure that an accurate lunar landing is not entirely dependent on Earth-based tracking systems.

The Safe and Precise Landing - Integrated Capabilities Evolution (SPLICE) project, a cross-disciplinary effort within NASA to develop precision landing and hazard avoidance technologies, is aiding in addressing this topic by investigating game-changing navigation and sensing techniques [3]. These efforts include developing simulation and analysis tools for evaluating candidate entry, descent, and landing (EDL) trajectories to near-term destinations such as the Moon and Mars [4]. In support of this mission, a novel sensor model for simulating Earth-based radiometric tracking measurements from DSN or DSN-like sites has been developed for use in linear covariance analysis – a rapid, early-stage tool for assessing guidance, navigation, and control (GN&C) system performance.

II. Linear Covariance Analysis Overview

Linear covariance methods for use in spacecraft and EDL applications have been detailed and demonstrated in [5–8] and are not considered a core finding or contribution of this effort, but a synopsis of these techniques will be presented for completeness. Assessing the overall performance of a GN&C system is a complex endeavor, often requiring the use of hundreds or thousands of Monte Carlo simulation runs to determine the desired statistical parameters. Broadly, linear covariance is an alternative or complementary approach to Monte Carlo analysis that produces similar statistical information for a closed-loop GN&C system in a single simulation run.

A. GN&C Performance Metrics

Before outlining the mathematical framework for linear covariance analysis, key performance metrics for evaluating a GN&C system must be defined. One of the primary concerns of this analysis lies in determining how well the vehicle can estimate its state and follow a desired trajectory. Figure 1 depicts the relationship between the nominal $\bar{\mathbf{x}}$, navigation/navigated $\hat{\mathbf{x}}$, true/actual $\mathbf{x}$, and design x states.

*GN&C Intern and Undergraduate Aerospace Engineering Student at the University of Kansas, bcollicott@ku.edu
†Aerospace Engineer, GN&C Autonomous Flight Systems Branch, david.c.woffinden@nasa.gov

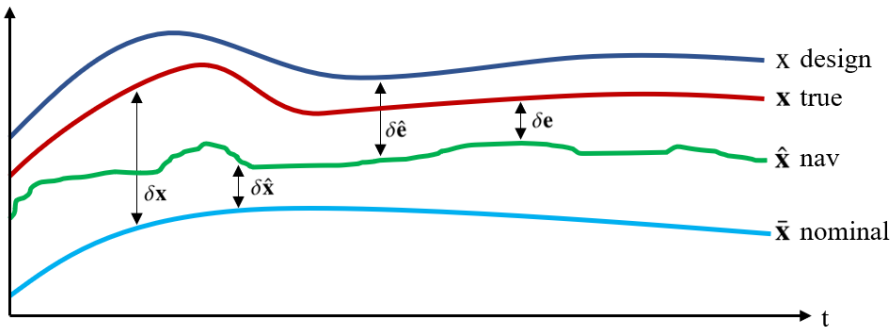

Fig. 1 GN&C Analysis Performance Metrics.

Between these states, the true dispersion $\delta\mathbf{x}$, which is also called the trajectory or environment dispersion, is defined as the difference between the true and nominal states. Similarly, the navigation dispersion $\delta\hat{\mathbf{x}}$ is the difference between the navigation and nominal states, and these dispersions also have associated covariance matrices, $\mathbf{D}$ and $\hat{\mathbf{D}}$, respectively.

$$\delta\mathbf{x} \triangleq \mathbf{x} - \bar{\mathbf{x}} \qquad \mathbf{D} = E\left[\,\delta\mathbf{x}\,\delta\mathbf{x}^{\mathrm{T}}\,\right] \tag{1}$$

$$\delta\hat{\mathbf{x}} \triangleq \hat{\mathbf{x}} - \bar{\mathbf{x}} \qquad \hat{\mathbf{D}} = E\left[\,\delta\hat{\mathbf{x}}\,\delta\hat{\mathbf{x}}^{\mathrm{T}}\,\right] \tag{2}$$

The covariance of the true dispersion characterizes the system's ability to follow a prescribed reference trajectory, and the covariance of the navigation dispersion quantifies how well the onboard system thinks that it can track the nominal trajectory.

In addition to dispersions defined relative to the nominal state, navigation $\delta\mathbf{e}$ and onboard $\delta\hat{\mathbf{e}}$ error may be computed relative to the navigation state.

$$\delta\mathbf{e} \triangleq \mathbf{x} - \hat{\mathbf{x}} \qquad \mathbf{P} = E\left[\,\delta\mathbf{e}\,\delta\mathbf{e}^{\mathrm{T}}\,\right] \tag{3}$$

$$\delta\hat{\mathbf{e}} \triangleq x - \hat{\mathbf{x}} \qquad \hat{\mathbf{P}} = E\left[\,\delta\hat{\mathbf{e}}\,\delta\hat{\mathbf{e}}^{\mathrm{T}}\,\right] \tag{4}$$

Since the navigation error represents the difference between the actual state and the navigation state, the covariance of the navigation error $\mathbf{P}$ represents the certainty with which the system estimates the true state. Similarly, the onboard error is defined as the difference between the design state and the navigation state, and its covariance $\hat{\mathbf{P}}$ describes the accuracy with which the onboard system predicts that it can estimate the design state assumed in the filter development. Note that the navigation error and onboard error are the same if the design and true states are assumed to be equal.

B. Computing Performance Metrics using Linear Covariance

The nominal reference trajectory $\bar{\mathbf{x}}$ is generated through the propagation of non-linear system dynamic models and GN&C algorithms, as illustrated in Fig. 2. Using this trajectory, the onboard covariance matrix $\hat{\mathbf{P}}$ and an augmented state covariance $\mathbf{C}$ are propagated, updated, and corrected. The augmented state covariance is comprised of a combination of the true dispersions $\delta\mathbf{x}$ and navigation dispersions $\delta\hat{\mathbf{x}}$:

$$\mathbf{C} = E\left[\,\delta\mathbf{X}\,\delta\mathbf{X}^{\mathrm{T}}\,\right] \tag{5}$$

$$\text{where} \qquad \delta\mathbf{X}^{\mathrm{T}} = \left[\,\delta\mathbf{x}^{\mathrm{T}}\;\delta\hat{\mathbf{x}}^{\mathrm{T}}\,\right] \tag{6}$$

For an n-dimensional true state vector and an n̂-dimensional navigation state vector, the mapping matrices shown in Eq. (7) are applied to the augmented covariance, yielding the environment dispersion $\mathbf{D}$, navigation dispersion $\hat{\mathbf{D}}$, and navigation error $\mathbf{P}$ covariance matrices.

$$\begin{aligned}
\mathbf{D} &= \left[\,\mathbf{I}_{n\times n}\;\mathbf{0}_{n\times\hat{n}}\,\right] \quad \mathbf{C}\left[\,\mathbf{I}_{n\times n}\;\mathbf{0}_{n\times\hat{n}}\,\right]^{\mathrm{T}} \\
\hat{\mathbf{D}} &= \left[\,\mathbf{0}_{\hat{n}\times n}\;\mathbf{I}_{\hat{n}\times\hat{n}}\,\right] \quad \mathbf{C}\left[\,\mathbf{0}_{\hat{n}\times n}\;\mathbf{I}_{\hat{n}\times\hat{n}}\,\right]^{\mathrm{T}} \\
\mathbf{P} &= \left[\,\mathbf{I}_{\hat{n}\times n}\;-\mathbf{I}_{\hat{n}\times\hat{n}}\,\right]\mathbf{C}\left[\,\mathbf{I}_{\hat{n}\times n}\;-\mathbf{I}_{\hat{n}\times\hat{n}}\,\right]^{\mathrm{T}}
\end{aligned} \tag{7}$$

Thus, performance metrics are calculated which may then be compared to the statistical results of other methods, such as the Monte Carlo analysis, to analyze a GN&C system and relevant mission trade studies.

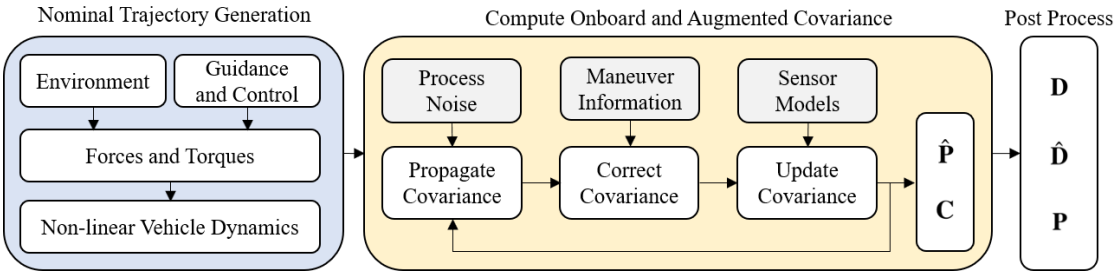

Fig. 2 Linear Covariance GN&C Analysis Flow Diagram

C. Sensor Modeling in a Linear Covariance Analysis

Details on implementing a discrete sensor model into the linear covariance analysis are presented here. Considering that sensor measurements are not actually computed using this analysis technique, sensor performance must be described in a way that contributes to updating the onboard and augmented covariance matrices. Consider a sensor measurement vector $\mathbf{z}$ and actual spacecraft state vector $\mathbf{x}$, which are related by the non-linear function $\mathbf{h}$:

$$\mathbf{z} = \mathbf{h}(\mathbf{x}, t) + \boldsymbol{\epsilon} \tag{8}$$

The function $\mathbf{h}$ represents the mathematical relationship between a noise-free observation and the true state. In this way, the term $\boldsymbol{\epsilon}$ accounts for error in the measurement, generally in the form of Gaussian white noise. This formulation may be linearized about reference state $\bar{\mathbf{x}}$ to produce the following expression as a function of the reference state and time:

$$\delta\mathbf{z} = \mathbf{H}(\mathbf{x}, t)\,\delta\mathbf{x} + \boldsymbol{\epsilon} \tag{9}$$

$$\text{where} \qquad \delta\mathbf{z} = \mathbf{z} - \bar{\mathbf{z}}\,, \quad \delta\mathbf{x} = \mathbf{x} - \bar{\mathbf{x}} \tag{10}$$

It can be seen that $\delta\mathbf{z}$ represents the deviation of actual measurements $\mathbf{z}$ from predicted measurements $\bar{\mathbf{z}}$ that are based on the reference state. Similarly, $\delta\mathbf{x}$ is a state deviation vector that quantifies the difference between the actual $\mathbf{x}$ and nominal $\bar{\mathbf{x}}$ states. The value of interest from this derivation is the $\mathbf{H}$-matrix, which represents the partial derivatives of the modeled observations (evaluated at the reference state $\bar{\mathbf{x}}$) with respect to the state vector $\mathbf{x}$ and is required to update both the onboard and augmented covariance matrices.

$$\mathbf{H}(\mathbf{x}, t) = \left.\frac{\partial \mathbf{h}(\mathbf{x}, t)}{\partial \mathbf{x}}\right|_{\mathbf{x}=\bar{\mathbf{x}}} \tag{11}$$

In summary, measurements are not computed in a linear covariance analysis; rather, the observations must be modeled in terms of state variables to compute the Jacobian $\mathbf{H}$-matrix at the time of each observation. Additionally, measurement noise and biases may be specified, as will be shown in the detailed derivation of the DSN sensor model. These sensors properties are used to update the onboard and augmented covariance matrices, allowing for the navigation performance and trajectory dispersion statistics to be computed.

III. Deep Space Network Measurement Model

This paper describes several methods for simulating radiometric tracking measurements in a linear covariance analysis. First, the mathematical model for range and range rate measurements is derived and implemented as an *onboard* sensor. Then, the modeling approach shifts to developing a batch processor, using weighted least squares and square root information filter formulations, to compute the state error using information from range and range rate measurements. The latter technique better approximates the operational usage of radiometric tracking measurements, in which an entire batch of data is processed before information is uplinked to the spacecraft. However, the onboard sensor approach still holds merit in it's simplicity and uniformity with other sensors used in covariance analysis. In both instances, the same model for measurements from Earth-based tracking stations is used. This model is heavily derived

from literature published by the NASA Jet Propulsion Laboratory (JPL), and information regarding general radiometric tracking, DSN measurement accuracy, sources of measurement error, and a wealth of technical details was retrieved from [9–13].

A. Math Model

The DSN sensor measurements depend on the spacecraft states of position $\mathbf{r}_{cg}$, velocity $\mathbf{v}_{cg}$, attitude, and attitude rate $\boldsymbol{\omega}_{cg}$, as well as external parameters such as ground station location $\mathbf{r}_{gs}$ and measurement biases b_ρ and $b_{\dot{\rho}}$. Spacecraft pointing error is accounted for using the estimated small angle rotation θ_{cg}, which is defined as the variation between the true body attitude and nominal body attitude. Therefore, when considering a tracking scenario with one active ground station, the portion of the state vector influencing the sensor measurement $\mathbf{x}$ of dimension 20×1 can be written as follows:

$$\mathbf{x}^{\mathrm{T}} = \begin{bmatrix} \mathbf{r}_{cg}^{\mathrm{T}} & \mathbf{v}_{cg}^{\mathrm{T}} & \theta_{cg}^{\mathrm{T}} & \boldsymbol{\omega}_{cg}^{\mathrm{T}} & \mathbf{r}_{a}^{\mathrm{T}} & \mathbf{r}_{gs}^{\mathrm{T}} & b_\rho & b_{\dot{\rho}} \end{bmatrix} \tag{12}$$

The spacecraft antenna arm $\mathbf{r}_a$ is included in the state vector due to it's impact on range and range rate measurements, as will be shown through further derivation.

DSN measurements primarily consist of slant range ρ, acquired by measuring the round-trip-light-time for a signal to travel from the ground station to the spacecraft, and range rate $\dot{\rho}$, which is computed by observing the doppler shift in incoming waves. These physical measurements must be expressed in terms of spacecraft state variables as depicted in Fig. 3, where a contextual diagram for computing the slant range to a spacecraft is shown.

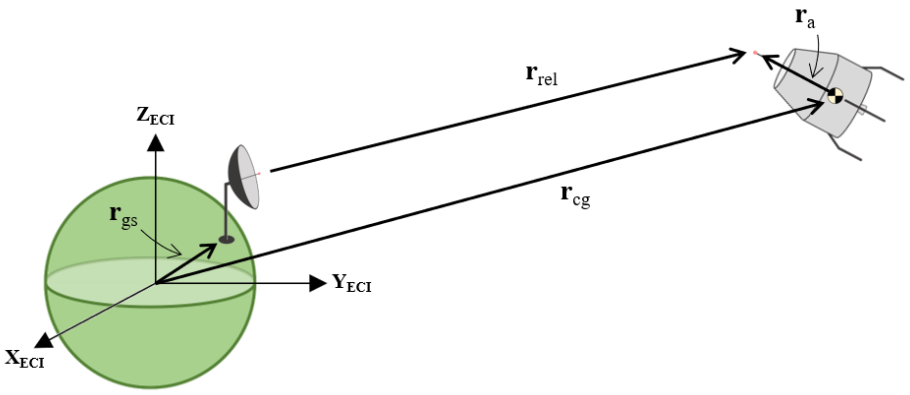

Fig. 3 Range Tracking Definition Sketch

The slant range may be defined as the magnitude of the line-of-sight relative position vector $\mathbf{r}_{rel}$, which is calculated as a combination of the spacecraft center-of-gravity $\mathbf{r}_{cg}$, spacecraft antenna $\mathbf{r}_a$, and ground station $\mathbf{r}_{gs}$ position vectors. Conventionally, all quantities should be computed in the Earth-Centered Inertial (ECI) reference frame.

$$\rho = \left| \mathbf{r}_{rel}^{i} \right| = \left| \mathbf{r}_{cg}^{i} + \mathbf{r}_{a}^{i} - \mathbf{r}_{gs}^{i} \right| \tag{13}$$

However, several of the quantities that comprise slant range are not natively known in the inertial frame, namely $\mathbf{r}_{gs}$ and $\mathbf{r}_a$, which are known in the Earth-Centered, Earth-Fixed (ECEF) and spacecraft body frames, respectively. Therefore, these components in the slant range formulation are transformed to the inertial reference frame.

$$\mathbf{r}_{a}^{i} = \mathbf{T}_{b}^{i}\, \mathbf{r}_{a}^{b}, \qquad \mathbf{r}_{gs}^{i} = \mathbf{T}_{p}^{i}\, \mathbf{r}_{gs}^{p} \tag{14}$$

Determining an expression for the ECEF-to-Inertial transformation matrix $\mathbf{T}_p^i$ requires knowledge of the relative orientation of planetary reference frames, whereas the nominal Body-to-Inertial transformation matrix $\mathbf{T}_b^i$ is obtained directly from the spacecraft attitude quaternion $\mathbf{q}_b^i$. In an effort to account for attitude dynamics, the formulation for $\mathbf{T}_b^i$ includes θ_{cg}^b, which represents the spacecraft's deviation from the nominal attitude state. Note that the nominal value for θ_{cg}^b is $\mathbf{0}_{3\times1}$ such that the transformation matrix is unaffected when evaluated at the reference state.

$$\mathbf{T}_{b}^{i} = \mathbf{T}_{\bar{b}}^{i}\, \mathbf{T}_{b}^{\bar{b}} = \mathbf{T}_{\bar{b}}^{i} \left(\mathbf{I} + \left[\theta_{cg}^{b} \times \right] \right) \tag{15}$$

The term $\left[\theta^{b}_{cg}\times\right]$ represents the 3×3 cross-product-equivalent matrix of the 3×1 vector θ^{b}_{cg}. By substituting Eqs. (14) and (15) into Eq. (13), the final expression for ρ may be written.

$$\rho \;=\; \left|\,\mathbf{r}^{i}_{cg} + \mathbf{T}^{i}_{\bar{b}}\left(\mathbf{I} + \left[\,\theta^{b}_{cg}\times\right]\right)\mathbf{r}^{b}_{a} - \mathbf{T}^{i}_{p}\,\mathbf{r}^{p}_{gs}\,\right| \tag{16}$$

An expression for range rate $\dot{\rho}$ is obtained by differentiating Eq. (13) with respect to time, resulting in the following:

$$\dot{\rho} \;=\; \frac{\left[\,\mathbf{v}^{i}_{rel}\,\right]^{T}\left[\,\mathbf{r}^{i}_{rel}\,\right]}{\left|\,\mathbf{r}^{i}_{rel}\,\right|} \;=\; \frac{\left[\,\mathbf{v}^{i}_{cg} + \mathbf{v}^{i}_{a} - \mathbf{v}^{i}_{gs}\,\right]^{T}\left[\,\mathbf{r}^{i}_{cg} + \mathbf{r}^{i}_{a} - \mathbf{r}^{i}_{gs}\,\right]}{\left|\,\mathbf{r}^{i}_{cg} + \mathbf{r}^{i}_{a} - \mathbf{r}^{i}_{gs}\,\right|} \tag{17}$$

Similar to the antenna and ground station terms in the slant range equation, antenna velocity $\mathbf{v}_a$ and ground station velocity $\mathbf{v}_{gs}$ may be expressed in terms of the body and planet-fixed reference frames, respectively. Additionally, the terms include the rotational velocity of the spacecraft $\boldsymbol{\omega}^{b}_{cg}$ and Earth $\boldsymbol{\omega}^{p}_{e}$ respectively. Assuming that the linear velocities of the antenna and ground station are zero in their native coordinate frames (i.e. rigid body motion), the rotation velocity component is the only contributor to their velocity.

$$\mathbf{v}^{i}_{a} \;=\; \boldsymbol{\omega}^{i}_{cg}\times\mathbf{r}^{i}_{a} \;=\; \mathbf{T}^{i}_{b}\left(\boldsymbol{\omega}^{b}_{cg}\times\mathbf{r}^{b}_{a}\right), \qquad \mathbf{v}^{i}_{gs} \;=\; \boldsymbol{\omega}^{i}_{e}\times\mathbf{r}^{i}_{gs} \;=\; \mathbf{T}^{i}_{p}\left(\boldsymbol{\omega}^{p}_{e}\times\mathbf{r}^{p}_{gs}\right) \tag{18}$$

By substituting Eqs. (14), (15), and (18) into Eq. (17), the final expression for $\dot{\rho}$ is obtained.

$$\dot{\rho} \;=\; \frac{\left[\,\mathbf{v}^{i}_{cg} + \mathbf{T}^{i}_{\bar{b}}\left(\mathbf{I} + \left[\,\theta^{b}_{cg}\times\right]\right)\left(\boldsymbol{\omega}^{b}_{cg}\times\mathbf{r}^{b}_{a}\right) - \mathbf{T}^{i}_{p}\left(\boldsymbol{\omega}^{p}_{e}\times\mathbf{r}^{p}_{gs}\right)\,\right]^{T}\left[\,\mathbf{r}^{i}_{cg} + \mathbf{T}^{i}_{\bar{b}}\left(\mathbf{I} + \left[\,\theta^{b}_{cg}\times\right]\right)\mathbf{r}^{b}_{a} - \mathbf{T}^{i}_{p}\,\mathbf{r}^{p}_{gs}\,\right]}{\left|\,\mathbf{r}^{i}_{cg} + \mathbf{T}^{i}_{\bar{b}}\left(\mathbf{I} + \left[\,\theta^{b}_{cg}\times\right]\right)\mathbf{r}^{b}_{a} - \mathbf{T}^{i}_{p}\,\mathbf{r}^{p}_{gs}\,\right|} \tag{19}$$

B. Implementation in Linear Covariance Analysis

Recalling Eq. (9), the previous section provides $\mathbf{h}(\mathbf{x}\,,t)$, the relationship between perfect observations and sensor state; therefore, the observation vector $\mathbf{z}$ is given as:

$$\mathbf{z} \;=\; \mathbf{h}(\mathbf{x}\,,t) \;=\; \begin{bmatrix}\rho\\ \dot{\rho}\end{bmatrix} + \mathbf{b} + \boldsymbol{\epsilon} \;=\; \begin{bmatrix}\tilde{\rho}\\ \tilde{\dot{\rho}}\end{bmatrix} \tag{20}$$

where the bias term $\mathbf{b}$ represents the measurement *uncertainty* in addition to the measurement noise $\boldsymbol{\epsilon}$. As shown in Eq. (11), $\mathbf{H}$ is the quantity of interest, so the observation vector $\mathbf{z}$ must be differentiated with respect to the state vector and evaluated at the nominal state (as indicated by the notation $\mathbf{x} = \bar{\mathbf{x}}$). The result of this operation is shown in Appendix A.

$$\mathbf{H}(\mathbf{x}_i\,,t_i) \;=\; \frac{\partial\mathbf{h}(\mathbf{x}_i\,,t_i)}{\partial\mathbf{x}_i}\bigg|_{\mathbf{x}_i=\bar{\mathbf{x}}_i} \;=\; \begin{bmatrix} \frac{\partial\tilde{\rho}}{\partial\mathbf{r}^{i}_{cg}} & \frac{\partial\tilde{\rho}}{\partial\mathbf{v}^{i}_{cg}} & \frac{\partial\tilde{\rho}}{\partial\theta^{i}_{cg}} & \frac{\partial\tilde{\rho}}{\partial\boldsymbol{\omega}^{i}_{cg}} & \frac{\partial\tilde{\rho}}{\partial\mathbf{r}^{b}_{a}} & \frac{\partial\tilde{\rho}}{\partial\mathbf{r}^{p}_{gs}} & \frac{\partial\tilde{\rho}}{\partial b_{\rho}} & \frac{\partial\tilde{\rho}}{\partial b_{\dot{\rho}}} \\ \frac{\partial\tilde{\dot{\rho}}}{\partial\mathbf{r}^{i}_{cg}} & \frac{\partial\tilde{\dot{\rho}}}{\partial\mathbf{v}^{i}_{cg}} & \frac{\partial\tilde{\dot{\rho}}}{\partial\theta^{i}_{cg}} & \frac{\partial\tilde{\dot{\rho}}}{\partial\boldsymbol{\omega}^{i}_{cg}} & \frac{\partial\tilde{\dot{\rho}}}{\partial\mathbf{r}^{b}_{a}} & \frac{\partial\tilde{\dot{\rho}}}{\partial\mathbf{r}^{p}_{gs}} & \frac{\partial\tilde{\dot{\rho}}}{\partial b_{\rho}} & \frac{\partial\tilde{\dot{\rho}}}{\partial b_{\dot{\rho}}} \end{bmatrix}_{\mathbf{x}=\bar{\mathbf{x}}} \tag{21}$$

The $\mathbf{H}$-matrix is computed at each time step as long as there is an unbroken line-of-sight between the ground station and spacecraft antenna. Figure 4 illustrates parameters used in determining the visibility from a ground station to spacecraft at arbitrary positions.

The angle θ between the ground station position vector $\mathbf{r}_{gs}$ and spacecraft contact point $\mathbf{r}_{sc}$ determines the line-of-sight for radio communications. If θ is larger than the 90°, then the ground station will be below the horizon and unable to observe the spacecraft. However, ground stations are limited to a minimum elevation angle at which measurement quality significantly degrades or the physical structure of the antenna does not support further declination. Therefore, for a spacecraft to be in view of a DSN station, the aforementioned angle θ must be less than a specified θ_{max}. It is convenient to use the cosine of the angle θ to check for line-of-sight, which is easily computed using the inner product between vectors.

$$\mathbf{r}^{i}_{sc} \;=\; \mathbf{r}^{i}_{cg} + \mathbf{r}^{i}_{a}\,, \qquad \cos\theta \;=\; \mathbf{r}^{i}_{gs}\cdot\mathbf{r}^{i}_{sc} \tag{22}$$

$$\text{DSN is in view when:} \qquad \cos\theta \;\geq\; \cos\theta_{max} \tag{23}$$

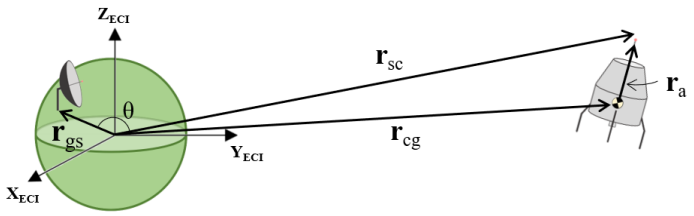

Fig. 4 Diagram for Checking Earth Obstruction of Spacecraft

It is also pertinent to check for line-of-sight obstruction by the Moon during lunar missions. Figure 5 provides definitions for variables used in determining line-of-sight contact for a spacecraft in proximity of the Moon. Using the definition for $\mathbf{r}_{sc}$ given in Eq. (23) and knowing the position of the Moon with respect to the ground station $\mathbf{r}_{m/gs}$, the position of the spacecraft with respect to the Moon $\mathbf{r}_{sc/m}$ may be computed. Therefore, the measurement validity may be determined geometrically.

$$\mathbf{r}^{i}_{sc/m} = \mathbf{r}^{i}_{sc} - \mathbf{r}^{i}_{m/gs}, \qquad r_{sc/m} = \left|\mathbf{r}^{i}_{sc/m}\right| \tag{24}$$

$$\text{therefore:} \quad b = \mathbf{r}^{i}_{sc/m} \cdot \frac{\mathbf{r}^{i}_{m/gs}}{r_{m/gs}} \quad \text{and} \quad h = \sqrt{r^2_{sc/m} - b^2} \tag{25}$$

$$\text{line-of-sight is obstructed when:} \quad b \geq 0 \quad \text{and} \quad h \leq r_m \tag{26}$$

The triangle's base, b, is computed as the vector projection of $\mathbf{r}_{sc/m}$ onto the unit vector $\hat{\mathbf{r}}_{m/gs}$, and the height, h, is found from Pythagorean's Theorem. Therefore, when the spacecraft is beyond the Moon ($b \geq 0$) and has less than one lunar radius of separation ($h \leq r_m$), the ground station can not track the spacecraft, and the measurement is invalid. The conditions for measurement validity from Eqs. (23) and (26) must be satisfied to obtain a measurement.

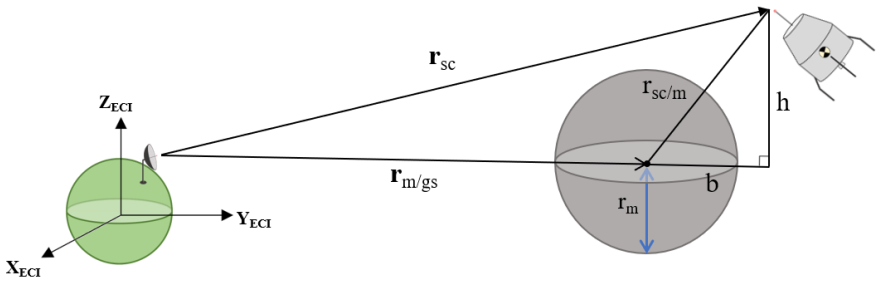

Fig. 5 Diagram for Checking Lunar Eclipse of Spacecraft

If the measurement is deemed valid at time t_i, then the matrix $\mathbf{H}_i$ is computed for the nominal state $\bar{\mathbf{x}}_i$ and used in computing new onboard and augmented covariances. There are two ways to implement measurements from DSN ground stations into a linear covariance simulation: as a range and range rate sensor that provides information for sequential processing *or* as a state estimate with a corresponding covariance that results from a batch processor. Both methods will be discussed below.

1. Onboard Sequential Processing

A simplified implementation of the DSN model in a linear covariance framework utilizes sequential processing of range ρ and range rate $\dot{\rho}$ measurement information as if directly available onboard the spacecraft. The **H**-matrix for a DSN measurement is calculated at the time epoch of each valid measurement and used to update the augmented covariance **C** and onboard covariance $\hat{\mathbf{P}}$. In addition to measurement partials, the sequential implementation also

requires assembly of the navigation and onboard filter measurement noise covariance $\mathbf{R}$ for use in determining the covariance of the measurement residual $\mathbf{R}_{\text{meas}}$. The sequential implementation utilizes several bias and noise terms; these values are specified in Table 1.

Table 1 Measurement Model Sources of Uncertainty (3σ)

Variable of Uncertainty		Bias Term	Noise Term
Range Measurement (m)	ρ	3.0	3.0
Range Rate Measurement (mm/s)	$\dot{\rho}$	0.03	0.03
Ground Station Position (cm)	$\mathbf{r}_{\text{gs}}^{\text{p}}$	5	–
Spacecraft Antenna Position (cm)	$\mathbf{r}_{\text{a}}^{\text{b}}$	30	–

The sequential implementation of a radiometric tracking sensor greatly simplifies the operational concept of such a model. Additionally, implementation into linear covariance only requires the definition of measurement error terms and partial derivatives to begin analyzing GN&C system performance. In this implementation, measurements as processed in a Kalman filter as they become available. This approach replicates the navigation performance that would result if each DSN measurement was processed in the onboard spacecraft filter, rather than on the ground. The updated onboard covariance is computed as a function of the Kalman gain $\mathbf{K}$, measurement partials $\mathbf{H}$, and measurement noise $\mathbf{R}$:

$$\hat{\mathbf{P}}_{i+1} = \mathbf{A}\,\hat{\mathbf{P}}_i\,\mathbf{A}^{\mathrm{T}} + \mathbf{K}\,\mathbf{R}\,\mathbf{K}^{\mathrm{T}} \tag{27}$$

$$\text{where} \quad \mathbf{K} = \hat{\mathbf{P}}_i\,\mathbf{H}_i^{\mathrm{T}}\,\mathbf{R}^{-1} \quad \text{and} \quad \mathbf{A} = \mathbf{I} - \mathbf{K}\,\mathbf{H}_i \tag{28}$$

Similarly, the augmented covariance matrix $\mathbf{C}$ may be computed using partials of the true measurement with respect to the true state $\mathbf{H}$ and estimated measurement with respect to the estimated state $\hat{\mathbf{H}}$:

$$\mathbf{C}_{i+1} = \mathbf{H}_{aug}\,\mathbf{C}_i\,\mathbf{H}_{aug}^{\mathrm{T}} + \mathbf{K}\,\mathbf{R}\,\mathbf{K}^{\mathrm{T}} \tag{29}$$

$$\text{where} \quad \mathbf{H}_{aug} = \begin{bmatrix} \mathbf{I} & \mathbf{0} \\ \mathbf{K}\mathbf{H} & \mathbf{I} - \mathbf{K}\hat{\mathbf{H}} \end{bmatrix} \tag{30}$$

2. External Batch Processing - Batch Least Squares

Sequential filtering provides a relatively simple, agile implementation of spacecraft radiometric tracking measurements; however, this approach does not reproduce the effect of processing measurements on the ground rather than onboard the spacecraft. In this implementation, a simple Batch Least Squares algorithm is used to process a batch of measurements and update the onboard covariance. The use of an *external filter* in processing measurements and informing navigation performance in a linear covariance analysis is considered a key contribution of this effort. The batch processor used in this DSN model is a Weighted Least Squares formulation similar to those found in [14] and [15]. In essence, the batch processor used specifically for DSN measurements is a secondary filter that runs in the background and provides information to the onboard filter once a tracking pass is complete.

Recall that the relationship between measurement observations $\mathbf{z}$ and spacecraft states $\mathbf{x}$ is linearized about some reference trajectory $\bar{\mathbf{x}}$ such that the relationship between measurement deviation $\delta\mathbf{z}$ and state deviation $\delta\mathbf{x}$ may be written as:

$$\delta\mathbf{z} = \mathbf{H}\,\delta\mathbf{x} + \boldsymbol{\epsilon} \tag{31}$$

Therefore, the measurement residual $\boldsymbol{\epsilon}$ represents the parameter to minimize in the Batch Least Squares formulation. The weighting matrix $\mathbf{W}$ is introduced in this definition and will be defined in later steps.

$$\boldsymbol{\epsilon} = \delta\mathbf{z} - \mathbf{H}\,\delta\mathbf{x} \tag{32}$$

$$\mathbf{J} = \frac{1}{2}\,\boldsymbol{\epsilon}^{\mathrm{T}}\,\mathbf{W}\,\boldsymbol{\epsilon} = \frac{1}{2}\left[\,\delta\mathbf{z} - \mathbf{H}\,\delta\mathbf{x}\,\right]^{\mathrm{T}}\mathbf{W}\left[\,\delta\mathbf{z} - \mathbf{H}\,\delta\mathbf{x}\,\right] \tag{33}$$

The least squares parameter $\mathbf{J}$ is minimized for the following conditions:

$$\frac{\partial\mathbf{J}}{\partial\mathbf{x}} = 0 \qquad \text{and} \qquad \frac{\partial^2\mathbf{J}}{\partial\mathbf{x}^2} > 0 \tag{34}$$

$$\text{such that:} \qquad \delta\tilde{\mathbf{x}} = \left(\mathbf{H}^{\mathrm{T}}\,\mathbf{W}\,\mathbf{H}\right)^{-1}\mathbf{H}^{\mathrm{T}}\,\mathbf{W}\,\delta\mathbf{z} \tag{35}$$

where $\delta\tilde{\mathbf{x}}$ represents the best estimate of actual state deviation vector $\delta\mathbf{x}$ based on the least squares method. By taking the weighting matrix $\mathbf{W}$ as the inverse of the measurement residual covariance $\mathbf{R}$, the covariance of the state estimate can be written for an unbiased estimate without *a priori* information.

$$\tilde{\mathbf{P}} \;=\; \mathrm{E}\Big\{ \big[\, \tilde{\mathbf{x}} - \mathrm{E}\{\,\tilde{\mathbf{x}}\,\} \,\big] \big[\, \tilde{\mathbf{x}} - \mathrm{E}\{\,\tilde{\mathbf{x}}\,\} \,\big]^{\mathrm{T}} \Big\} \;=\; \mathrm{E}\Big\{ \big[\, \tilde{\mathbf{x}} - \mathbf{x} \,\big] \big[\, \tilde{\mathbf{x}} - \mathbf{x} \,\big]^{\mathrm{T}} \Big\} \;=\; \left(\mathbf{H}^{\mathrm{T}}\, \mathbf{R}^{-1}\, \mathbf{H}\right)^{-1} \tag{36}$$

The value of interest in this derivation is the covariance of the state estimate $\tilde{\mathbf{P}}$ – once this covariance matrix is obtained for a batch of data, the existing onboard covariance is updated with this new information to represent the certainty with which the spacecraft knows its state. Consider a batch of an arbitrary number of observations to be used in estimating the state of the spacecraft at the final observation time. To use information from previous measurements in estimating the current state, the $\mathbf{H}$-matrices must be made relevant to the time of interest through the use of state transition matrices Φ.

$$\mathbf{x}_{i+1} \;=\; \Phi(t_{i+1},\, t_i)\, \mathbf{x}_i \qquad , \quad \Phi(t_{i+1},\, t_i) \;=\; \frac{\partial \mathbf{x}_{i+1}}{\partial \mathbf{x}_i} \tag{37}$$

$$\text{such that:} \qquad \tilde{\mathbf{H}}_i \;=\; \mathbf{H}(\mathbf{x}_i,\, t_i)\, \Phi(t_k,\, t_i)\,, \quad \mathbf{P}_k \;=\; \Phi(t_k,\, t_i)\, \mathbf{P}_i\, \Phi(t_k,\, t_i)^{\mathrm{T}} \tag{38}$$

An $\mathbf{H}$-matrix that has been advanced to the time of the batch update is denoted as $\tilde{\mathbf{H}}$. The state transition matrix $\Phi(t_i,\, t_{i-1})$ from t_{i-1} to t_i is obtained by numerically integrating the expression in Eq. (39). In this application, the ordinary differential equation in Eq. (39) is jointly integrated with the state vector using a fourth-order Runge-Kutta scheme.

$$\dot{\Phi}(t_{i+1},\, t_i) = \mathbf{A}(\mathbf{x}_i,\, t_i)\, \Phi(t_{i+1},\, t_i) \tag{39}$$

$$\text{where } \dot{\mathbf{x}}_i \qquad\quad = \mathbf{A}(\mathbf{x}_i,\, t_i)\, \mathbf{x}_i \tag{40}$$

The spacecraft state vector $\mathbf{x}$ contains k instances of epoch-specific spacecraft state vectors. The sensor state vector has the dimension $n \times 1$ and is dependent on the number of ground stations such that $n = 17 + 3n_{\mathrm{gs}}$. Similarly, the observation vector $\mathbf{z}$ contains two scalar measurements (range and range rate) per ground station at each time step such that $z = 2n_{\mathrm{gs}}$, and it follows that the error terms are of compatible dimensions. The unbiased, perfect observations are represented by Eqs. (16) and (19) evaluated at the reference state $\bar{\mathbf{x}}$. These equations were differentiated with respect to the sensor state to obtain the $\mathbf{H}$-matrix.

$$\mathbf{h}(\mathbf{x},\, t) \;=\; \begin{bmatrix} \rho \\ \dot{\rho} \end{bmatrix} \;=\; \begin{bmatrix} \Big|\, \mathbf{r}^{\mathrm{i}}_{\mathrm{cg}} + \mathbf{T}^{\mathrm{i}}_{\bar{\mathrm{b}}} \left(\mathbf{I} + \left[\, \theta^{\mathrm{b}}_{\mathrm{cg}} \times \,\right] \right) \mathbf{r}^{\mathrm{b}}_{\mathrm{a}} - \mathbf{T}^{\mathrm{i}}_{\mathrm{p}}\, \mathbf{r}^{\mathrm{p}}_{\mathrm{gs}} \,\Big| \\ \dfrac{\left[\, \mathbf{v}^{\mathrm{i}}_{\mathrm{cg}} + \mathbf{T}^{\mathrm{i}}_{\bar{\mathrm{b}}} \left(\mathbf{I} + \left[\, \theta^{\mathrm{b}}_{\mathrm{cg}} \times \,\right] \right) (\boldsymbol{\omega}^{\mathrm{b}}_{\mathrm{cg}} \times \mathbf{r}^{\mathrm{b}}_{\mathrm{a}}) - \mathbf{T}^{\mathrm{i}}_{\mathrm{p}}\, (\boldsymbol{\omega}^{\mathrm{p}}_{\mathrm{e}} \times \mathbf{r}^{\mathrm{p}}_{\mathrm{gs}}) \,\right]^{\mathrm{T}} \left[\, \mathbf{r}^{\mathrm{i}}_{\mathrm{cg}} + \mathbf{T}^{\mathrm{i}}_{\bar{\mathrm{b}}} \left(\mathbf{I} + \left[\, \theta^{\mathrm{b}}_{\mathrm{cg}} \times \,\right] \right) \mathbf{r}^{\mathrm{b}}_{\mathrm{a}} - \mathbf{T}^{\mathrm{i}}_{\mathrm{p}}\, \mathbf{r}^{\mathrm{p}}_{\mathrm{gs}} \,\right]}{\Big|\, \mathbf{r}^{\mathrm{i}}_{\mathrm{cg}} + \mathbf{T}^{\mathrm{i}}_{\bar{\mathrm{b}}} \left(\mathbf{I} + \left[\, \theta^{\mathrm{b}}_{\mathrm{cg}} \times \,\right] \right) \mathbf{r}^{\mathrm{b}}_{\mathrm{a}} - \mathbf{T}^{\mathrm{i}}_{\mathrm{p}}\, \mathbf{r}^{\mathrm{p}}_{\mathrm{gs}} \,\Big|} \end{bmatrix} \tag{41}$$

The Batch Least Squares is generally an iterative process that begins with a nominal trajectory $\bar{\mathbf{x}}$ and is carried out until an adequate state estimate $\tilde{\mathbf{x}}_k$ is obtained. However, measurements are not truly computed in a linear covariance analysis and a state estimate is not obtained. Rather, this batch filter formulation only computes the covariance and cannot iterate. For the batch of data, the covariance of the state estimate $\tilde{\mathbf{P}}_k$ is computed with *a priori* covariance $\mathbf{P}^-_k$ in addition to the expression from Eq. (36).

$$\tilde{\mathbf{P}}_k \;=\; \left(\sum_{i=0}^{k} \tilde{\mathbf{H}}_i^{\mathrm{T}}\, \mathbf{R}_i^{-1}\, \tilde{\mathbf{H}}_i + (\,\mathbf{P}^-_k\,)^{-1} \right)^{-1} \tag{42}$$

Although a batch least squares processor may be sufficient for determining a state estimate in a real-world orbit determination problem, this formulation does not incorporate stochastic processes such as process noise and therefore lends itself to procucing overly optimistic covariance values. This combined with concerns of numerical stability resulted in conversion to factorized filter formulations in deep space tracking applications [16]. The following section details the implementation of a factorized filter that includes *time updates* to incorporate process noise and compute a covariance that appropriately characterizes the statistics of orbit determination via radiometric tracking.

3. External Batch Processing - Square Root Information Filter

The square-root information filter (SRIF) formulation of the least-squares method, which operates on the square root factor of the inverse of the covariance matrix, is applied here to incorporate process noise and ensure numerical stability of the solution. The SRIF formulation in [17] was adopted for this application. Again, this formulation was adapted by linear covariance analysis by eschewing the state estimate and only computing the square-root factor $\mathbf{S}$ of the information matrix at each measurement time.

$$\tilde{\mathbf{P}} = \mathbf{\Lambda}^{-1} = \mathbf{S}^{-1}\mathbf{S}^{-\mathrm{T}} \tag{43}$$

The square-root matrix is obtained via Cholesky decomposition of the information matrix $\mathbf{\Lambda}$. In the SRIF algorithm, the measurement equation is normalized using the Cholesky factor of the measurement noise covariance $\mathbf{R}^{1/2}$, necessitating normalization of the $\mathbf{H}$-matrix in this application.

$$\mathbf{H} = \mathbf{R}^{-1/2}\mathbf{H}_{orig} \tag{44}$$

To incorporate process noise, a new state transition equation is written in place of Eq. (37) that includes the state process noise $\mathbf{w}$ and a process noise mapping matrix $\Gamma(t_{i+1},\, t_i)$.

$$\mathbf{x}_{i+1} = \Phi(t_{i+1},\, t_i)\mathbf{x}_i + \Gamma(t_{i+1},\, t_i)\mathbf{w}_i \tag{45}$$

An approximation for the process noise mapping matrix Γ is obtained using the system input dynamics $\mathbf{B}$ and computing the first-order of the Peno-Baker expansion for the state transition matrix Φ. The state vector $\mathbf{x}$ includes a generalized constant variable C to account for additional, unchanging states, and each matrix entry in the following derivation represents a 3×3 block.

$$\dot{\mathbf{x}} = \mathbf{A}\mathbf{x} + \mathrm{B}\mathbf{w}, \qquad \mathbf{x} = \begin{bmatrix} \mathbf{r}_{\mathrm{cg}}^{\mathrm{T}} & \mathbf{v}_{\mathrm{cg}}^{\mathrm{T}} & \theta_{\mathrm{cg}}^{\mathrm{T}} & \boldsymbol{\omega}_{\mathrm{cg}}^{\mathrm{T}} & C^{\mathrm{T}} \end{bmatrix}^{\mathrm{T}}, \qquad \mathbf{w} = \begin{bmatrix} \mathbf{w}_{\mathbf{v}_{\mathrm{cg}}}^{\mathrm{T}} & \mathbf{w}_{\boldsymbol{\omega}_{\mathrm{cg}}}^{\mathrm{T}} \end{bmatrix}^{\mathrm{T}}$$

$$\mathbf{A} = \begin{bmatrix} \mathbf{0} & \mathbf{I} & \mathbf{0} & \mathbf{0} & \mathbf{0} \\ \mathbf{G} & \mathbf{0} & \mathbf{0} & \mathbf{0} & \mathbf{0} \\ \mathbf{0} & \mathbf{0} & \left[\, \boldsymbol{\omega}_{\mathrm{cg}}\times \right] & \mathbf{I} & \mathbf{0} \\ \mathbf{0} & \mathbf{0} & \mathbf{0} & \left[\, \boldsymbol{\omega}_{\mathrm{cg}}^{*} \right] & \mathbf{0} \\ \mathbf{0} & \mathbf{0} & \mathbf{0} & \mathbf{0} & \mathbf{0} \end{bmatrix} \quad \mathbf{B} = \begin{bmatrix} \mathbf{0} & \mathbf{0} \\ \mathbf{I} & \mathbf{0} \\ \mathbf{0} & \mathbf{0} \\ \mathbf{0} & \mathbf{I} \\ \mathbf{0} & \mathbf{0} \end{bmatrix} \quad \Phi(t_{i+1},\, t_i) \approx \mathbf{I} + \mathbf{A}\Delta\mathrm{t} = \begin{bmatrix} \mathbf{I} & \mathbf{I}\Delta\mathrm{t} & \mathbf{0} & \mathbf{0} & \mathbf{0} \\ \mathbf{G}\Delta\mathrm{t} & \mathbf{I} & \mathbf{0} & \mathbf{0} & \mathbf{0} \\ \mathbf{0} & \mathbf{0} & \mathbf{I} + \left[\, \boldsymbol{\omega}_{\mathrm{cg}}\times \right]\Delta\mathrm{t} & \mathbf{I} & \mathbf{0} \\ \mathbf{0} & \mathbf{0} & \mathbf{0} & \mathbf{I} + \left[\, \boldsymbol{\omega}_{\mathrm{cg}}^{*} \right]\Delta\mathrm{t} & \mathbf{0} \\ \mathbf{0} & \mathbf{0} & \mathbf{0} & \mathbf{0} & \mathbf{I} \end{bmatrix}$$

$$\text{for constant process noise, } \Gamma(t_{i+1},\, t_i) \approx \int_{t_i}^{t_{i+1}} \Phi(t_{i+1},\, \tau)\mathbf{B}(\tau)\mathrm{d}\tau = \begin{bmatrix} \mathbf{I}\frac{\Delta\mathrm{t}^2}{2} & \mathbf{0} \\ \mathbf{I}\Delta\mathrm{t} & \mathbf{0} \\ \mathbf{0} & \mathbf{I}\Delta\mathrm{t} \\ \mathbf{0} & \mathbf{I}\Delta\mathrm{t} + \left[\, \boldsymbol{\omega}_{\mathrm{cg}}^{*} \right]\frac{\Delta\mathrm{t}^2}{2} \\ \mathbf{0} & \mathbf{0} \end{bmatrix} \tag{46}$$

The matrix $\mathbf{G}$ represents the gravity gradient acting on the spacecraft, and the notation $\boldsymbol{\omega}_{\mathrm{cg}}^{*}$ represents a function of spacecraft attitude rate $\boldsymbol{\omega}_{\mathrm{cg}}$ and moment of inertia matrix $\mathbf{I}_{\mathrm{sc}}$.

$$\left[\, \boldsymbol{\omega}_{\mathrm{cg}}^{*} \right] = \mathbf{I}_{\mathrm{sc}}^{-1}\left[\, (\mathbf{I}_{\mathrm{sc}}\, \boldsymbol{\omega}_{\mathrm{cg}})\times \right] - \mathbf{I}_{\mathrm{sc}}^{-1}\left[\, \boldsymbol{\omega}_{\mathrm{cg}}\times \right]\mathbf{I}_{\mathrm{sc}} \tag{47}$$

For a process noise vector with q elements, the $q \times q$ process noise error covariance $\mathbf{Q}$ can be obtained and factored into its respective square-root information terms.

$$\mathbf{Q} = \mathbf{S}_w^{-1}\mathbf{S}_w^{-\mathrm{T}} \tag{48}$$

The Householder algorithm is used in carrying out both the time update and the measurement update, and this process is denoted using a representative matrix $\mathbf{T}$ that produces an upper triangular matrix. This notation is exemplified using arbitrary matrix $\mathbf{M}$ in Eq. (49)

$$\mathbf{T}\,\mathbf{M} = \hat{\mathbf{M}} \tag{49}$$

The SRIF algorithm, including process noise, is shown in Table 2 for a batch of k measurements with *a priori* square-root information matrix $\mathbf{S}_k^-$.

Table 2 Square Root Information Filter Algorithm

for $i = 1, 2, \ldots, k$	
Normalize H-matrix using measurement noise:	$\mathbf{H}_i = \mathbf{R}_i^{-1/2}\,\mathbf{H}_i$
Measurement update using n Householder transformations:	$\hat{\mathbf{T}}_i \begin{bmatrix} \mathbf{S}_i^- \\ \mathbf{H}_i \end{bmatrix} = \begin{bmatrix} \hat{\mathbf{S}}_i \\ \mathbf{0} \end{bmatrix}$
Time update from t_i to t_{i+1}:	$\mathbf{S}_{i+1} = \hat{\mathbf{S}}_i \Phi^{-1}(t_{i+1},\, t_i)$
Incorporate process noise using q Householder transformations:	$\bar{\mathbf{T}}_i \begin{bmatrix} \mathbf{S}_{w_i} & \mathbf{0} \\ -\mathbf{S}_{i+1}\Gamma(t_{i+1},\, t_i) & \mathbf{S}_{i+1} \end{bmatrix} = \begin{bmatrix} \mathbf{S}^-_{w_{i+1}} & \mathbf{S}^-_{w_{i+1}x_{i+1}} \\ \mathbf{0} & \mathbf{S}^-_{i+1} \end{bmatrix}$
	set $\quad i = i + 1$
end for	
compute covariance:	$\tilde{\mathbf{P}}_k = \hat{\mathbf{S}}_k^{-1} \hat{\mathbf{S}}_k^{-\mathrm{T}}$

There are two approaches to outputting the information from an external ground-based filter, such as the SRIF, to the onboard filter in a linear covariance analysis. The upper-left 6×6 block of the state estimate covariance $\tilde{\mathbf{P}}_k$ can be output as the measurement error $\mathbf{R}$ accompanied by a 6×6 identity $\mathbf{H}$-matrix for use in a measurement update to the onboard covariance as shown in Eq. (27) and augmented covariance as in Eq. (29). In this way, the range and range rate measurements are mapped directly to information on the spacecraft's position and velocity for processing in the onboard filter. Alternatively, the new state estimate may be used to replace the previous covariance by overwriting the onboard filter state estimate and associated covariance. In this case, the covariance of the position and velocity navigation error are reset to the values output by the SRIF filter. Recalling Eqn. (3), the navigation error is defined as the difference bewteen the nominal state and navigation state. Combining this expression with Eqns. (1) and (2) shows that the navigation error can also be expressed in terms of the true dispersion and navigation dispersions.

$$\hat{\mathbf{P}}^+ = E\left[\, [\delta\mathbf{e}^+]\, [\delta\mathbf{e}^+]^{\mathrm{T}} \,\right] = \tilde{\mathbf{P}}_k \tag{50}$$

$$\delta\mathbf{e}^+ = \delta\mathbf{x}^- - \delta\hat{\mathbf{x}}^+ \rightarrow \delta\hat{\mathbf{x}}^+ = \delta\mathbf{e}^+ - \delta\mathbf{x}^- \tag{51}$$

By leaving the true dispersion $\delta\mathbf{x}$ unchanged, the new navigation dispersion $\delta\hat{\mathbf{x}}^+$ may be computed and used in updating the augmented covariance matrix. This *reset* process was derived and explored in depth in [18, 19].

$$\mathbf{C}^+ = E\left[\, [\delta\mathbf{x}^- \delta\hat{\mathbf{x}}^+]\, [\delta\mathbf{x}^- \delta\hat{\mathbf{x}}^+]^{\mathrm{T}} \,\right] \tag{52}$$

A summary of options for integrating DSN measurement information into linear covariance analysis is shown in Fig. 6.

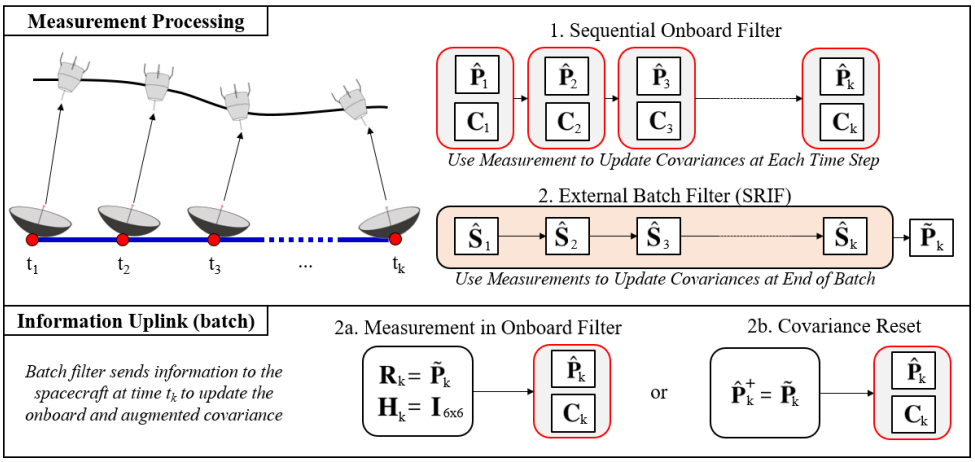

Fig. 6 DSN Measurement Processing Options

IV. Alternative Methods

Despite the longstanding history of radiometric tracking in spacecraft navigation, alternate techniques are currently being fielded to reduce the burden on Earth-based antenna networks and improve navigation precision for future missions. This paper aims to provide a comparison of the TRN model outlined in [20] with the DSN model presented in the previous section in order to shed light on the effectiveness of both systems as standalones and complements. This effort investigates the use of a high-altitude optical camera for visual detection of surface features. Any subset of 1500 known feature on the Moon can be included in the onboard database for use in analysis. The model includes constraints for sunlight incidence angle, camera field of view, distance to the feature, and vehicle velocity. As a result, the performance of this TRN system is heavily dependent on the trajectory profile and time epoch of the mission. This sensor provides information to the onboard filter in the form of a bearing measurement to the visible feature. The sensor specifications used in this analysis are shown alongside the TRN definition sketch in Fig. 7.

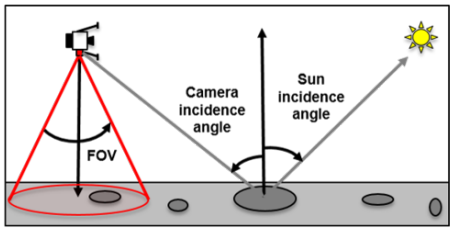

Camera Bearing Noise	0.005	deg
Camera Bearing Bias	0.2	deg
Camera Mounting Misalignment	0.2	deg
Camera Field-of-View	60	deg
Max/Min Sun Incidence Angle	85/0	deg
Feature Location Bias	20	m

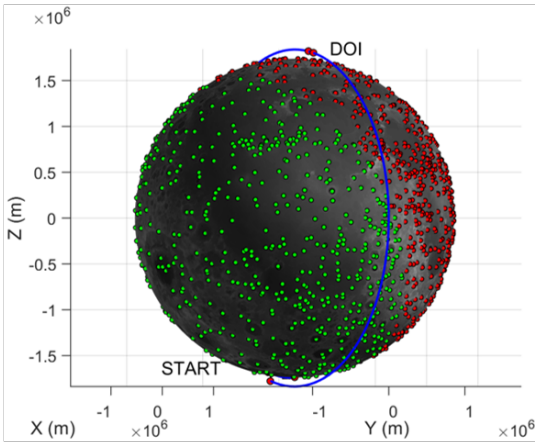

Fig. 7 Terrain Camera Sensor Definition Sketch and Specifications (3σ)

V. Lunar Descent and Landing Navigation Analysis

Analysis of near-term lunar surface missions are of primary importance to the SPLICE program. This analysis utilizes three lunar trajectories that could serve as the holding orbit before descent and landing. Equatorial and polar trajectories were selected for their candidacy in upcoming lunar missions, and a third *maximum visibility* orbit was determined in which the line-of-sight from Earth-based ground stations would never be impeded by the moon. These three trajectory profiles are shown in Fig. 8. Each scenario begins in a 100×100km circular orbit with a de-orbit insertion (DOI) burn after 1, 2, or 3 orbital revolutions that reduces the spacecraft's altitude to 15km, where powered descent initiation (PDI) is assumed to occur. Since DSN tracking primarily affects navigation performance at DOI and PDI, further stages of descent and landing are not simulated or analyzed in this study. As shown in the trade study matrix (Table 3), the mission profile is modified to include additional revolutions in orbit around the Moon prior to DOI. In cases where the TRN system is active, features are detected and processed throughout the entire simulation, whereas DSN tracking measurements are limited to pre-DOI. Every combination of the variables in Table 3 was explored for a total of 414 simulations to draw results from. Significant findings are examined in the following section.

Table 3 Trade Study Parameters

Processing Method	Trajectory	No. Revolutions	No. Ground Stations	No. TRN Features
Reset, Measurement	Polar, Equatorial, Max Vis.	1, 2, 3	0, 1, 2, 3, 6, 9	0, 500, 1000, 1500

The ground stations were set to measure range and range rate at an interval of 100 seconds between measurements. If the vehicle was eclipsed by the moon, the batch of measurements would resume when the spacecraft line-of-sight was restored. For each scenario, the DSN uplink was provided to the spacecraft one minute before DOI. Before examining

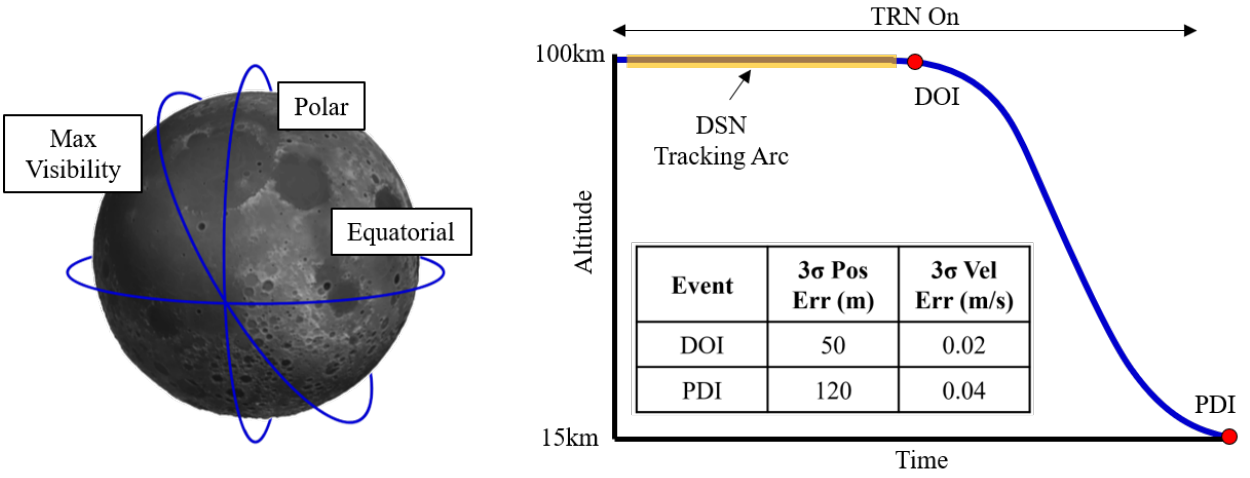

Event	3σ Pos Err (m)	3σ Vel Err (m/s)
DOI	50	0.02
PDI	120	0.04

Fig. 8 DSN Trade Study Orbits and Representative Results

results, it is pertinent to understand the visibility pattern of the selected ground stations. Figure 9 shows an example of the time history of ground station contact with the spacecraft in the initial 100×100km orbit for 24 hours. Only seven unique tracking facilities were identified with overlapping visibility, so additional sites were activated at DSN Goldstone and Madrid to reach a total of nine ground stations. The ground stations are shown in the order (from top to bottom) that they were selected for use in trade studies – e.g., if three ground stations were activated, then stations in Fairbanks, Goldstone, and White Sands would be available for tracking.

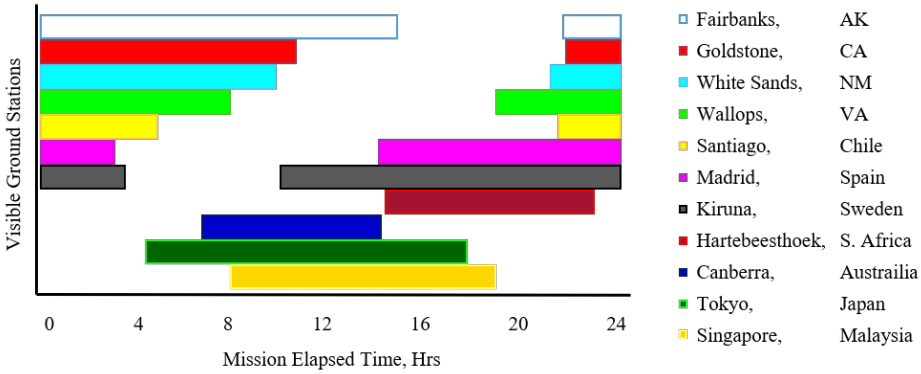

Fig. 9 Ground Station Visibility for Selected Trajectories

Simulation results were obtained for navigation performance at both DOI and PDI for DSN and TRN systems as shown in Fig. 8. The results for DSN-only simulations were computed using the *reset* method, whereas the DSN and TRN combination runs necessitated the use of the *measurement* update method. Using the reset method in the latter case would fail to take into account the information provided by the TRN system when uplinking DSN measurement information to the spacecraft – for this reason, the resulting information from the external DSN filter was treated as a measurement to be processed by the onboard filter alongside any relative navigation measurements.

VI. Results

Selected results will be analyzed here with emphasis on the single-revolution scenarios, as additional revolutions in orbit did not definitively improve navigation performance. The one revolution results for Maximum Visibility, Polar, and Equatorial orbits are shown in Figs. 10, 11, and 12 respectively. The general trend in each figure is consistent - additional ground stations enhance navigation performance but with marginal return for each ground station beyond

3. A sample of the DSN-only performance for each trajectory is provided in Table 4 to highlight the consistent 30% decrease in position error when increasing the number of active ground stations from 3 to 9. Also consistent throughout the results is the performance improvement due to synergy with TRN measurements. It can be seen graphically that when using a TRN in conjunction with ground tracking, the decrease in position and velocity error is similar to that of utilizing an additional ground station; however, the equatorial case highlights the dependence of TRN performance on environmental conditions by showing the lowest position error at DOI, but the highest position error at PDI for TRN cases. Also shown in Table 4 is the TRN performance at DOI, further indicating that the equatorial trajectory allowed the vehicle to encounter more features at this specific mission time.

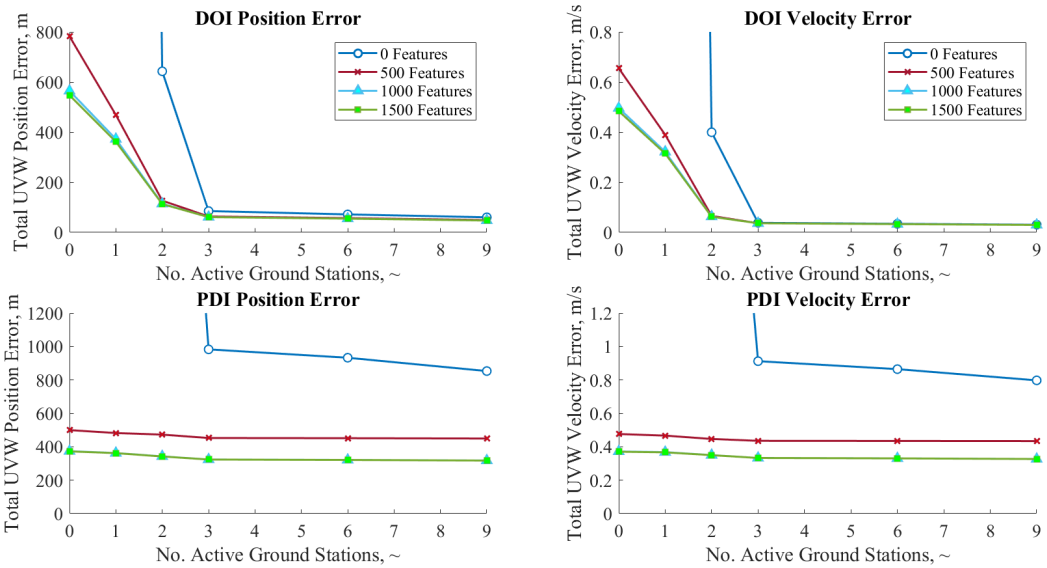

Fig. 10 Max Visibility Trajectory, Single Orbit Navigation Error at DOI and PDI

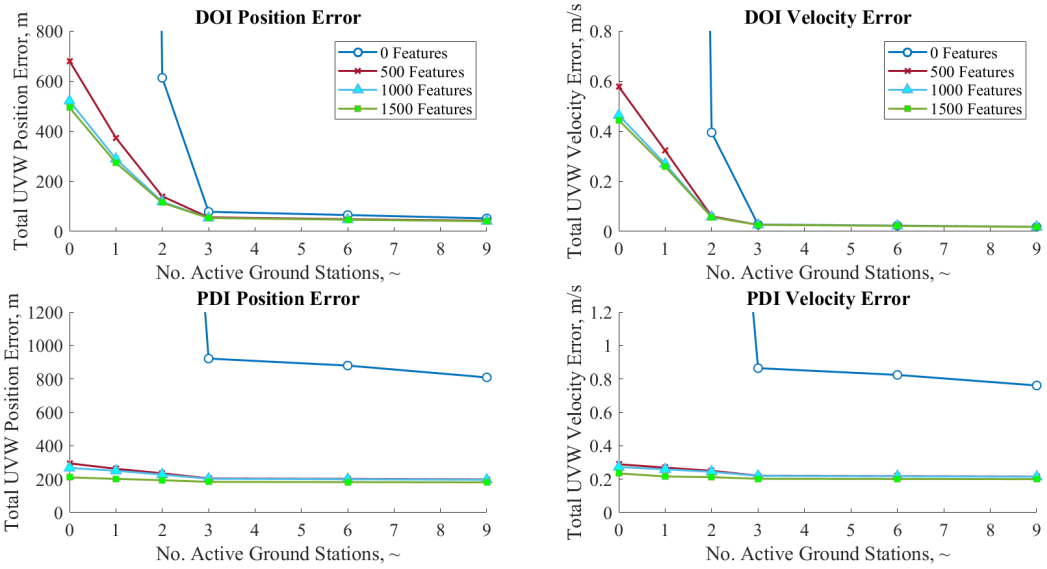

Fig. 11 Polar Trajectory, Single Orbit Navigation Error at DOI and PDI

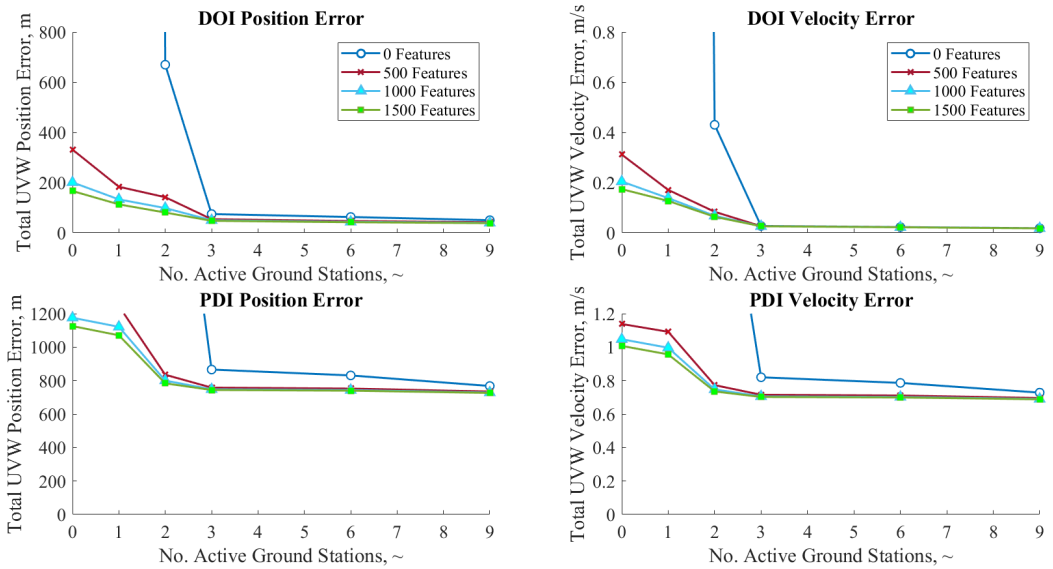

Fig. 12 Equatorial Trajectory, Single Orbit Navigation Error at DOI and PDI

Table 4 DSN and TRN Standalone Performance, One Orbit Revolution

DSN-only at DOI				
	3 Ground Stations		9 Ground Stations	
	3σ Pos Error (m)	3σ Vel Error (m/s)	3σ Pos Error (m)	3σ Vel Error (m/s)
Max Visibility	85.2	0.04	60.3	0.03
Polar	78.2	0.03	51.8	0.02
Equatorial	74.8	0.03	50.3	0.02
TRN-only with 1500 Feature Database				
	DOI		PDI	
	3σ Pos Error (m)	3σ Vel Error (m/s)	3σ Pos Error (m)	3σ Vel Error (m/s)
Max Visibility	547.2	0.48	499.7	0.48
Polar	494.0	0.44	210.9	0.23
Equatorial	166.5	0.17	1125.6	1.01

VII. Conclusion

This paper outlined the development of a novel ground-based radiometric tracking sensor model for use in linear covariance analysis in support of NASA's Safe and Precise Landing – Integrated Capabilities Evolution project. Linear covariance analysis provides an agile method for evaluating the performance of a GN&C system, and the addition of a radiometric tracking model advances the capability of this powerful tool to investigate sensor suites and define requirements for descent and landing missions. The relevance of this contribution is underscored by the numerous near-term Lunar missions currently evaluating the necessity of Deep Space Network measurements for a successful lunar landing. Additionally, this sensor model allows for comparative analysis with proposed alternatives, such as terrain relative navigation.

This radiometric tracking model takes into account uncertainties that affect range and range rate measurements as well as spacecraft attitude dynamics to accurately capture the performance of ground-based tracking systems. This

study highlights the significant nuance present in determining the trajectory and timing that achieve the best radiometric tracking performance. Although this study is best treated as an informative exercise that highlights the general trends associated with radiometric and terrain-relative navigation methods, the following conclusions can be drawn from simulation data: (1) At least three geometrically-diverse ground stations are required to achieve high accuracy (<100 m position error) with radiometric tracking alone. (2) The tracking measurement problem is geometrically driven and highly dependent on the relative orientation and motion of the spacecraft and ground stations. (3) Additional revolutions in orbit (i.e. additional tracking passes) do not always improve navigation precision. (4) A TRN system most significantly augments navigation performance when few (n<3) ground stations are available. There is significant challenge in determining the integrated performance of a GN&C system. As such, the development of novel simulation tools such as this DSN model in an agile linear covariance framework will expedite analysis into the capabilities and limitations of human landing systems for near-term space missions.

Appendix A: H-Matrix Partial Derivatives

$$\frac{\partial \rho}{\partial \mathbf{r}^{i}_{cg}} = \left[\hat{\mathbf{r}}^{i}_{rel}\right]^{T} \qquad \frac{\partial \dot{\rho}}{\partial \mathbf{r}^{i}_{cg}} = \frac{\left[\mathbf{v}^{i}_{rel}\right]^{T}}{\left|\mathbf{r}^{i}_{rel}\right|}\left(\left[\mathbf{I}\right] - \left[\hat{\mathbf{r}}^{i}_{rel}\right]\left[\hat{\mathbf{r}}^{i}_{rel}\right]^{T}\right)$$

$$\frac{\partial \rho}{\partial \mathbf{v}^{i}_{cg}} = 0 \qquad \frac{\partial \dot{\rho}}{\partial \mathbf{v}^{i}_{cg}} = \left[\hat{\mathbf{r}}^{i}_{rel}\right]^{T}$$

$$\frac{\partial \rho}{\partial \Theta^{b}_{cg}} = -\left[\hat{\mathbf{r}}^{i}_{rel}\right]^{T}\left[\mathbf{T}^{i}_{b}\right]\left[\mathbf{r}^{b}_{a}\times\right] \qquad \frac{\partial \dot{\rho}}{\partial \Theta^{b}_{cg}} = \frac{\left[\mathbf{v}^{i}_{rel}\right]^{T}}{\left|\mathbf{r}^{i}_{rel}\right|}\left(\left[\hat{\mathbf{r}}^{i}_{rel}\right]\left[\hat{\mathbf{r}}^{i}_{rel}\right]^{T} - \left[\mathbf{I}\right]\right)\left[\mathbf{T}^{i}_{b}\right]\left[\mathbf{r}^{b}_{a}\times\right] - \left[\hat{\mathbf{r}}^{i}_{rel}\right]^{T}\left[\mathbf{T}^{i}_{b}\right]\left[\mathbf{v}^{b}_{a}\times\right]$$

$$\frac{\partial \rho}{\partial \boldsymbol{\omega}^{b}_{cg}} = 0 \qquad \frac{\partial \dot{\rho}}{\partial \boldsymbol{\omega}^{b}_{cg}} = -\left[\mathbf{r}^{i}_{rel}\right]^{T}\left[\mathbf{T}^{i}_{b}\right]\left[\mathbf{r}^{b}_{a}\times\right]$$

$$\frac{\partial \rho}{\partial \mathbf{r}^{b}_{a}} = \left[\hat{\mathbf{r}}^{i}_{rel}\right]^{T}\left[\mathbf{T}^{i}_{b}\right] \qquad \frac{\partial \dot{\rho}}{\partial \mathbf{r}^{b}_{a}} = \frac{\left[\mathbf{v}^{i}_{rel}\right]^{T}}{\left|\mathbf{r}^{i}_{rel}\right|}\left(\left[\mathbf{I}\right] - \left[\hat{\mathbf{r}}^{i}_{rel}\right]\left[\hat{\mathbf{r}}^{i}_{rel}\right]^{T}\right)\left[\mathbf{T}^{i}_{b}\right] + \left[\hat{\mathbf{r}}^{i}_{rel}\right]^{T}\left[\mathbf{T}^{i}_{b}\right]\left[\boldsymbol{\omega}^{b}_{cg}\times\right]$$

$$\frac{\partial \rho}{\partial \mathbf{r}^{p}_{gs}} = -\left[\hat{\mathbf{r}}^{i}_{rel}\right]^{T}\left[\mathbf{T}^{i}_{p}\right] \qquad \frac{\partial \dot{\rho}}{\partial \mathbf{r}^{p}_{gs}} = \frac{\left[\mathbf{v}^{i}_{rel}\right]^{T}}{\left|\mathbf{r}^{i}_{rel}\right|}\left(\left[\hat{\mathbf{r}}^{i}_{rel}\right]\left[\hat{\mathbf{r}}^{i}_{rel}\right]^{T} - \left[\mathbf{I}\right]\right)\left[\mathbf{T}^{i}_{p}\right] - \left[\hat{\mathbf{r}}^{i}_{rel}\right]^{T}\left[\mathbf{T}^{i}_{p}\right]\left[\boldsymbol{\omega}^{p}_{e}\times\right]$$

$$\frac{\partial \rho}{\partial b_{\rho}} = 1 \qquad \frac{\partial \dot{\rho}}{\partial b_{\rho}} = 0$$

$$\frac{\partial \rho}{\partial b_{\dot{\rho}}} = 0 \qquad \frac{\partial \dot{\rho}}{\partial b_{\dot{\rho}}} = 1$$

Acknowledgments

This work was completed through an opportunity under NASA Internships Cooperative Agreement NNX13AJ37A in conjunction with the University Space Research Association (USRA). B. C. Collicott would like to thank the individuals from USRA and SPLICE who orchestrated this internship opportunity as well as James McCabe, Chris D'Souza, and other members of the Aeroscience and Flight Mechanics Division at NASA Johnson Space Center for their insight and guidance in developing the DSN model.

References

[1] Mudgway, D. J., *Uplink-Downlink: A History of the Deep Space Network*, No. SP-2001-4227 in The NASA History Series, NASA Office of External Relations, Washington, DC, 2001.

[2] Steffes, S. R., Barton, G. H., Bhatt, S. A., Fritz, M. P., King, E. T., and Woffinden, D. C., "Deep Space Autonomous Navigation Options for Future NASA Crewed Missions," AAS 18-083, Breckenridge, CO, February 2018. https://doi.org/10.2514/6.2017-5369.

[3] Carson, J. M., Munk, M. M., Sostaric, R. R., Estes, J. N., Amzajerdian, F., B., B. J., Rutishauser, D. K., Restrepo, C. I., Dwyer Cianciolo, A., Chen, G. T., and Tse, T., "The SPLICE Project: Continuing NASA Development of GN&C Technologies for Safe and Precise Landing," AIAA SciTech 2019, San Diego, CA, January 2019. https://doi.org/10.2514/6.2019-0660.

[4] Dwyer Cianciolo, A., Dutta, S., Lugo, R., Williams, A., and Chen, P., "A Simulation Framework for Precision Landing and Hazard Avoidance Technology," AIAA SciTech 2020, Orlando, FL, January 2020. https://doi.org/10.2514/6.2020-0366.

[5] Geller, D. K., "Linear Covariance Techniques for Orbital Rendezvous Analysis and Autonomous Onboard Mission Planning," *Journal of Guidance, Navigation, and Control*, Vol. 29, No. 6, November–December 2006. https://doi.org/10.2514/1.19447.

[6] Geller, D. K., and Christensen, D. P., "Linear Covariance Analysis for Powered Lunar Descent and Landing," *Journal of Spacecraft and Rockets*, Vol. 46, No. 6, November–December 2009. https://doi.org/10.2514/1.38641.

[7] Woffinden, D. C., Robinson, S. B., Williams, J. W., and Putnam, Z. R., "Linear Covariance Analysis Techniques to Generate Navigation and Sensor Requirements for the Safe and Precise Landing – Integrated Capabilities Evolution (SPLICE) Project," AIAA SciTech 2019, San Diego, CA, January 2019. https://doi.org/10.2514/6.2019-0662.

[8] Williams, J. W., Woffinden, D. C., and Putnam, Z. R., "Mars Entry Guidance and Navigation Analysis Using Linear Covariance Techniques for the Safe and Precise Landing – Integrated Capabilities Evolution (SPLICE) Project," AIAA SciTech 2020, Orlando, FL, January 2020. https://doi.org/10.2514/6.2020-0597.

[9] Thornton, C. L., and Border, J. S., *Radiometric Tracking Techniques for Deep-Space Navigation*, JPL Publication 00-11 in Deep-Space Communications and Navigation Series, NASA Jet Propulsion Laboratory, Pasadena, CA, October 2000.

[10] *DSN Telecommunications Link Design Handbook*, DSN 810-005, JPL Publication D-18379, Rev. E, NASA Jet Propulsion Laboratory, Pasadena, CA, December 2019.

[11] *Deep Space Network Services Catalog*, DSN 820-100, JPL Publication D-19002, Rev. F, NASA Jet Propulsion Laboratory, Pasadena, CA, February 2015.

[12] Hamilton, T. W., and Melbourne, W. G., "Information Content of a Single Pass of Doppler Data from a Distant Spacecraft," *Space Programs Summary*, Vol. III, No. 37-39, March–April 1966, pp. 18–24.

[13] Sovers, O. J., and Jacobs, C. S., *Observation Model and Parameter Partials for the JPL VLBI Parameter Estimation Software MODEST*, JPL Publication 83-39, Rev. 5, NASA Jet Propulsion Laboratory, Pasadena, CA, 1994.

[14] Tapley, B. D., Schutz, B. E., and Born, G. H., *Statistical Orbit Determination*, Elsevier Academic Press, Burlington, MA, 2004.

[15] Montenbruck, O., and Gill, E., *Satellite Orbits*, Springer-Verlag Berlin Heidelberg, Berlin, Germany, 2000.

[16] Lichten, S. M., *Estimation and Filtering Techniques for High-Accuracy GPS Applications*, Telecommunications and Data Acquisition Progress Report 42-97, NASA Jet Propulsion Laboratory, Pasadena, CA, 1989.

[17] D'Souza, C., "On the Square Root Information Filter (SRIF) and Square Root Information Smoother (SRIS) Formulation," January 2016.

[18] Woffinden, D., and Breger, L., "Automated Derivation and Verification of Navigation Requirements for On-Orbit Rendezvous," AIAA Guidance, Navigation, and Control Conference, Boston, MA, August 2013. https://doi.org/10.2514/6.2013-4964.

[19] Zanetti, R., Woffinden, D., and Sievers, A., "Multiple Event Triggers in Linear Covariance Analysis for Spacecraft Rendezvous," *Journal of Guidance, Control, and Dynamics*, Vol. 35, No. 2, 2012, pp. 353–366. https://doi.org/10.2514/1.54965.

[20] Dwyer Cianciolo, A., Striepe, S., Carson, J., Sostaric, R., Woffinden, D., Karlgaard, C., Lugo, R., Powell, R., and Tynis, J., "Defining Navigation Requirements for Future Precision Lander Missions," AIAA SciTech 2019, San Diego, CA, January 2019. https://doi.org/10.2514/6.2019-0661.